High-fidelity post-impact residual strength assessment for composite aircraft sustainment

K. Jacobs[1] , A.B. Harman[2], R.B. Ladani[1], R. Das[1] and A.C. Orifici[1]

[1]School of Engineering, RMIT University, Melbourne, Australia and [2]Defence Science and Technology Group, Fishermans Bend, VIC, Australia
Corresponding author: K. Jacobs; Email: s3485498@student.rmit.edu.au

Abstract

High-fidelity simulation tools have significant potential to support composite aircraft sustainment, though further study is required on incorporating the complex impact damage field. In this paper, compressive residual strength assessment is investigated using the high-fidelity computational tool BSAM™. The experimental impact damage was mapped and modelled at a high-fidelity level, which included ply-by-ply definition of the geometry of the impact indentation, fibre fracture in the plies and delamination in ply interfaces. It was shown that applying a small lateral displacement or 'pseudo-impact' step was highly effective in generating matrix cracks in the impact region, which provided a suitably realistic representation of the interconnected damage map through-the-thickness. It was found that inclusion of all damage modes in the post-image damage map at a high-fidelity definition was essential due to the strong degree of interaction between damage modes. The results support improved sustainment of defence platforms, through enhanced predictive capability and understanding.

Nomenclature

Symbol	Definition
E_1	Elastic modulus in the fibre direction
E_2/E_3	Elastic modulus in the in-plane and out-of-plane transverse directions
F_{GT}/F_{GC}	Shape parameter used to define CDM response of model in tension and compression respectively. This parameter is used to define percentage of fracture energy dissipated by the initial fibre fracture compared to the progressive fibre fractures.
F_{XT}/F_{XC}	Shape parameter used to define CDM response of model in tension and compression respectively. This parameter is used to define percentage of strength at which progressive fibre fractures continue.
G_{12}	Shear modulus in the 1-2 plane
G_{13}	Shear modulus in the 1-3 plane
G_{23}	Shear modulus in the 2-3 plane
G_{Ic}	Mode I interlaminar fracture toughness
G_{IIc}	Mode II interlaminar fracture toughness
G_{XT}/G_{XC}	Fibre fracture energy in tension and compression, respectively. Total energy released due to progressive fibre fracture.
S	In-plane shear strength in the 1-2 plane
X_C	Ultimate compressive strength in the fibre direction
X_T	Ultimate tensile strength in the fibre direction
Y_C	Ultimate compressive strength in the in-plane transverse direction
Y_T	Ultimate tensile strength in the in-plane transverse direction
ν_{12}	Poisson's ratio in the 1-2 plane

| ν_{13} | Poisson's ratio in the 1-3 plane |
| ν_{23} | Poisson's ratio in the 2-3 plane |

1.0 Introduction

Fibre-reinforced composites are becoming heavily used in modern aircraft. Composites are prone to damage caused by small impacts, such as dropped tools or rocks. This damage is typically in the form of matrix cracking, fibre breakage and delamination, which can be barely visible or invisible without equipment. The impact leads to significant reduction in structural strength, hence, predicting the residual strength of composite structures in operation is fundamental to sustainment of defence platforms.

Current analytical tools for composite structures are more limited than their metallic counterparts. This is particularly so for predicting residual strength after impact damage for in-service aircraft, as this requires a deep understanding and high-fidelity representation of damage modes and structural behaviour. The residual compressive strength of composites after impact is driven by a complex combination of multiple damage modes (delamination, matrix crack, fibre failure), coupled with complex structural effects (buckling and out-of-plane deformation, impact damage patterns) [1].

Composite damage modes have been represented by a wide range of strategies in finite element analysis (FEA), with one common distinction necessary between strategies that explicitly model damage as a crack and those that represent the effect of damage as a reduction in material properties such as stiffness in strength. Delamination is typically represented using explicit crack modelling approaches, such as virtual crack closure technique (VCCT) or cohesive zone modelling (CZM) [2], where fracture energy is used as the criterion to control separation between two crack planes. In contrast, continuum damage mechanics (CDM) [3] is a broad framework, which involves predicting damage and reducing material properties and is commonly used to capture matrix cracking and fibre fracture damage. However, CDM is not able to represent the crack opening effect, which presents limitations in capturing the interaction between damage modes. Some authors have used explicit crack modelling approaches (similar to those used for delamination) for modelling matrix cracking, in an approach referred to broadly as discrete damage modelling (DDM) [4].

Several studies have applied a range of techniques to capture the damage progression and static compressive residual strength of composite laminates. Some of these techniques include simulating a low-velocity impact event, coupled with a static analysis of a compression after impact (CAI) test [5–10]. Other studies have compared scans of impacted specimens to determine a generic set of shapes that are common in impacted specimen [11–13]. Soutis et al. took scans of a damaged specimen and imported a delamination map to a static CAI numerical prediction [1]. Bull et al. created a similar delamination map and also measured the deformation caused by the impact and modelled the deformation into the geometry of the model [14]. McQuien et al. combined both these methods and introduced an initial step to induce matrix cracking around the mapped damage [15]. From these, it can be seen that successful prediction of compressive residual strength requires high-fidelity physically representative capture of damage modes and their interaction. For example, delamination and matrix cracking cause physical separation and sharp cracks that initiate further damage and can interact and link together. Realistic representation of impact damage (delamination and fibre fracture map as well as geometry effects such as indentation) is critical to residual strength.

The high-fidelity computational tool BSAM™ contains various damage models that make it suitable for a DDM approach to predicting performance of composite structures, such as static CAI strength [16, 17]. Delamination is incorporated through the use of a CZM that operates between interfaces and can be used to model cohesive contact between plies. Fibre fracture is incorporated through an in-plane ply damage model that is based on CDM. Matrix cracking is incorporated through an in-plane ply damage model that introduces a mesh independent crack (MIC). This is initiated using a failure criterion (such as the LaRC04, from NASA [18]) and results in an explicit crack being introduced within the element, which itself is governed by a CZM. The crack formulation is framed using the Regularized
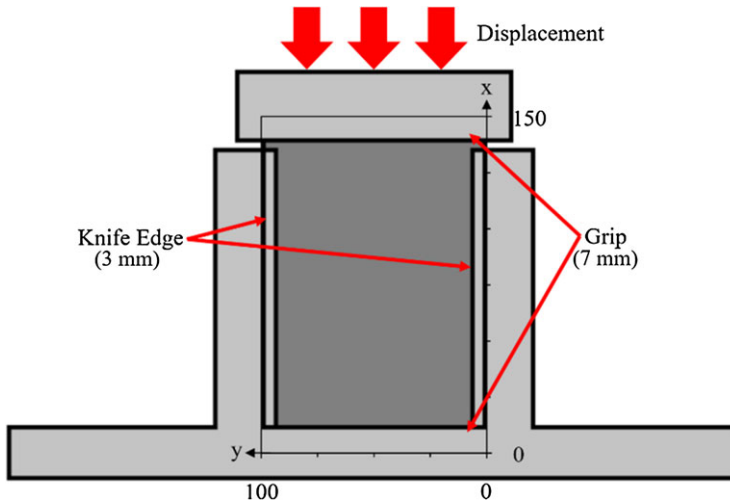
Figure 1. *Compression-sfter-impact test dimensions and schematic.*

eXtended Finite Element Method (RxFEM) [16, 17], which uses a continuous function to split the element and introduce a MIC, instead of a discontinuous function as used in the eXtended Finite Element Method (XFEM) [16, 17].

In previous work, Harman et al. used BSAM™ to analyse the residual strength and damage behaviour of compression after impact specimens [19]. The analysis incorporated the impact-induced dent and delamination zones in each ply interface and achieved strength predictions within 4%. However, the fibre fracture and matrix cracking caused by the impact were not included, and a detailed summary of the damage behaviour was not presented.

In this paper, the analysis strategy of Harman et al. [19] is extended to include an out-of-plane displacement pre-load step to create a network of matrix cracking as part of the impact damage. A detailed investigation is conducted into capturing the fibre fracture from impact, in terms of developing a modelling strategy and the influence on the damage behaviour and residual strength. The progression of damage modes leading to ultimate failure is investigated, and interaction of damage modes is studied. The outcomes of the work have application to improving the sustainment of defence platforms, through enhanced predictive capability and material understanding leading to reductions in costs in maintenance and operation of aircraft with composite structures.

2.0 Experimental testing

The experimental testing in this work used CAI specimens (Fig. 1) to focus on residual strength of composites with barely visible impact damage (BVID). The experimental testing was completed previously at Defence Science and Technology Group (DSTG) [19]. An intermediate-modulus carbon fibre with a toughened epoxy resin composite material system was used in this work, which is typical of new generation aircraft. The material was used in a 32-ply stacking sequence of $[45/0/-45/90]_{4S}$ with a cured laminate total thickness of 4mm. The testing configuration can be seen in Fig. 1. The specimen dimensions and testing configuration followed the American Society for Testing Materials (ASTM) D7137/D7137M compression after impact test [20]. The experimental procedure was conducted on nine specimens that were impacted with a 16mm spherical tup of 4.69kg mass at an impact energy of 8.14 J. A typical specimen underwent X-ray microfocus computed tomography (XmCT) scans to capture the damage patterns caused by the impact.

All specimens were fitted into a test fixture and displaced at a loading rate of 1mm/min in an Instron (model 1345, USA) test machine. Three 350Ω 3mm axial strain gauges (KFG-3-350-C1-11, Kyowa,

Table 1. *Material properties*

Elastic constants		Transverse strengths (CZM and MIC)		Fibre fracture (CDM)	
E_1 (MPa)	207,000	Y_T (MPa)	60	X_T (MPa)	1,847
E_2, E_3 (MPa)	8,300	Y_C (MPa)	200	X_C (MPa)	973
G_{23} (MPa)	2,000	S (MPa)	51	$G_{XT}/G_{XC}*$	80/18
G_{13}, G_{12} (MPa)	3,400	G_{Ic} (kJ/m^2)	0.213	$F_{XT}/F_{XC}*$	0.4
ν_{23}	0.4	G_{IIc} (kJ/m^2)	0.726	$F_{GT}/F_{GC}*$	0.4
ν_{13}, ν_{12}	0.13				

*Properties used for numerical prediction; explanation included in table of nomenclature.

Japan) were used to measure the far-field strain. Specimens were tested quasi-statically to failure, where the peak load was considered the 'failure load' for each specimen. One specimen was interrupted at approximately 95% of the failure load. This was determined by observing specimens during testing and using notable events as markers for approximate load percentages, (i.e. multiple "pinging" sounds occur as the specimen approaches failure, typically occurring above 90% load, and increasing in frequency past 95% load). As it is not possible to test the failure load of the interrupted specimen, a minimal value of 95% failure load was used. The interrupted specimen was removed from the fixture to undergo XmCT scans.

3.0 Finite element models

The high-fidelity RxFEM tool BSAM™ developed by Iarve and Mollenhaur [16, 17] was applied. To achieve an accurate prediction the delamination, matrix cracking and fibre fracture all must be captured. To capture these damage modes the following techniques were utilised:

- Delamination captured by using a CZM at every ply interface.
- In-plane matrix cracking captured using MIC, where a displacement discontinuity in the ply is introduced that includes a CZM.
- In-plane fibre fracture using CDM to soften ply elements.

The set of properties controlling these damage modes can be found in the corresponding columns of Table 1.

The mesh used in the model was created with the boundary conditions in mind. The loading grips on the top and bottom of the experimental specimen were measured at 7.5mm. These zones (marked red on Fig. 2) in the model were constrained in all directions on one end and in all directions except the displacement loading in the x-direction on the other as shown. The sides of the experimental specimen were secured with knife edges 3mm in from either edge to prevent global buckling. These knife edges were represented in the model by constraining the out-of-plane z displacement of the nodes marked in blue (Fig. 2) on the front and back surfaces of the model. The unloaded edges of the specimen were fixed in the y direction to represent the walls of the fixture (marked green in Fig. 2). The finite elements used in the model were C3D8, an eight-node solid element, with a mesh length of 0.8mm in the centre, 2.5mm in the outer region and 4-mm at the top and bottom. Each ply used a single layer of elements, leading to 10,382 nodes and 5,106 elements per ply and a total of 332,224 nodes and 163,392 elements. A cohesive zone was applied between each ply. The mesh used was similar to that of previous studies [19] and is based on ensuring a suitably small length for proper operation of the damage models. Several other mesh refinements were investigated (Table 2). Reducing the mesh sizing led to only a 2.5% difference in load with no noticeable difference in damage patterns while increasing the mesh sizing load to a 6.9% difference in load and the damage pattern remained relatively unchanged. A similar change was found increasing the mesh sizing further. The mesh sizing was completed using the damage techniques,

Table 2. *Mesh sizing chart, compared to 0.8mm failure load*

Damage zone mesh size (mm)	Number of elements	Load % of 0.8mm
0.6	218,368	102.5%
0.8	163,392	100%
1.2	113,632	106.9%
1.6	90,176	107.6%
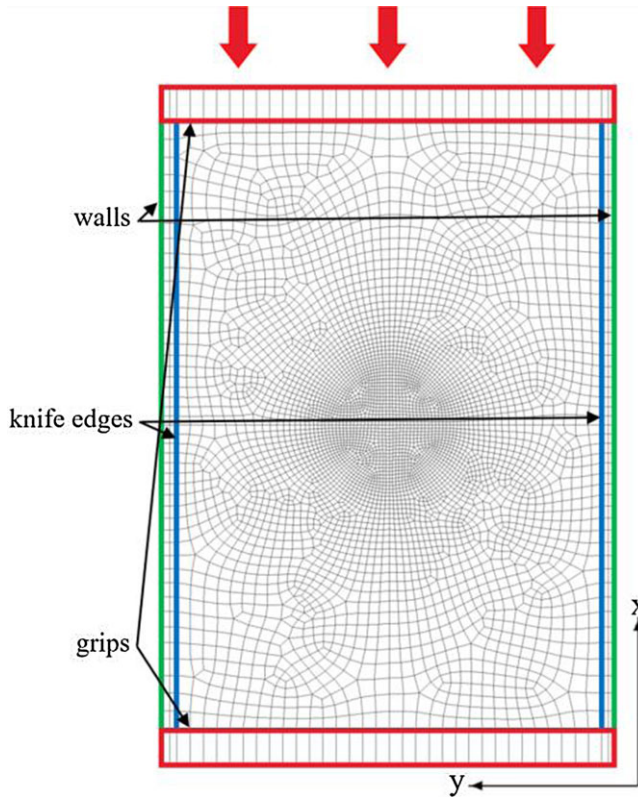
Figure 2. *Mesh and boundary conditions.*

explained later in this work, to ensure these were taken into account when considering limitations. Due to this it was determined that the optimal sizing for capturing a damage map and damage progression using the Rx-FEM software is approximately 0.8mm within the damage zone.

4.0 Damage mapping

Non-destructive testing post-impact was used to experimentally characterise the damage, including ultrasonic inspection and XmCT. This impact damage was then mapped into the model in the form of a dent, delamination zones and fibre fracture regions.

4.1 Indentation

The formation of the dent was achieved using methods developed in previous work [19], where the nodes are displaced in height (z) based on experimental observations to capture the deformed shape of the dent. This involved using XmCT scans to find the depth of the dent and measuring the diameter of
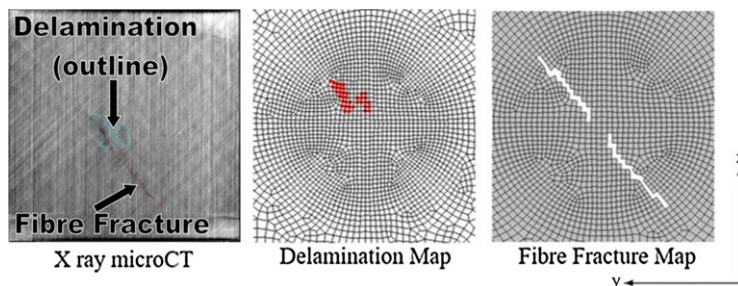
Figure 3. *Sample XmCT of the first interface [19] (left) and corresponding delamination (middle) and fibre fracture (right) map.*

the dent. The depth on the impact face was found to be 0.25 and 0.125mm on the impact and back faces, respectively. The diameter of the dent was found to be 40mm on the impact face and 50mm on the back. This dent shape was then applied to the mesh using cosine functions that were interpolated between the front and back faces (Fig. 4).

4.2 Delamination

The ply interfaces are represented using a CZM connection between each ply. The XmCT scans were used to identify delamination zones within each interface. These zones were then mapped to node sets within the model (e.g. red regions in the delamination map in Fig. 3). Two node sets were created for each ply, one using the bonded nodes and one for the debonded nodes (delaminated). A separate interface was applied to each of these node sets, with standard material properties applied to the bonded interface, and a set of weakened properties were applied to the debonded interface. The weakened properties used involved reducing the interface strengths as low as 0.5% of the full material strengths, allowing separation to occur during the early stages of the loading cycle without causing a divergence in the model.

4.3 Fibre fracture

The fibre fracture caused by the impact was modelled as an explicitly defined crack. This was achieved by creating a crack path out of the XmCT scans and translating it across to the mesh for the corresponding ply. All elements that intersected with this crack path were then deleted from the model. Given the fine mesh in the impact region this led to a thin crack with a sharp edge (e.g. see the fibre fracture map, Fig. 3). Mesh sensitivity studies confirmed that the damage progression and overall panel failure load were not affected by mesh at this level of refinement, and the fibre fracture CDM damage model also incorporates energy-based softening to alleviate mesh sensitivity issues in damage progression.

4.4 Matrix cracking

The matrix cracks cannot be mapped directly to the model from the scans as they are too fine to be mapped accurately. Instead, a small out-of-plane displacement was applied to the model to initiate matrix cracking, which typically occurs around the other mapped damage. This technique is called pseudo-impact and has been used in previous work by McQuien et al. [15]. The pseudo-impact technique as implemented by applying an out-of-plane displacement in the direction of the impact. This displacement was applied to a node set on the impact face that was the same diameter as the impactor tup (16mm). The displacement was selected based on creating a suitable distribution of matrix cracks, with a focus on ensuring that the MIC connected to delamination locations. This created a suitable network
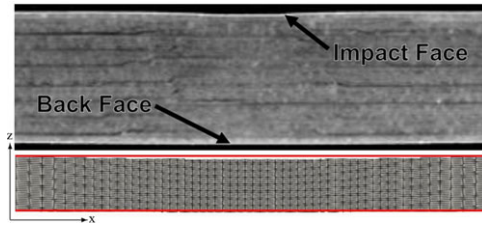
Figure 4. *XmCT of the indentation [19] (top) and cross-section of the mesh (bottom).*
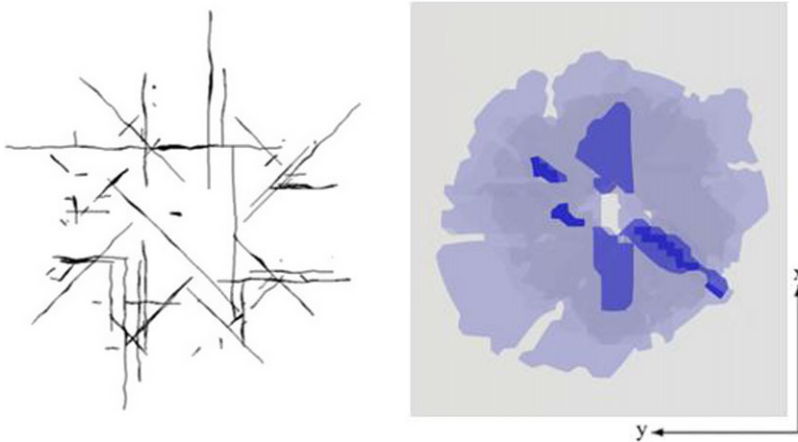

Figure 5. *Sample stack (combining all plies) of matrix cracks (left) and delaminations (right).*

of interconnecting damage between matrix cracks and delamination, similar to that seen in experiment (e.g. see the cross-section image in Fig. 4). It was also ensured that no extra damage occurred during the pseudo-impact displacement in the form of fibre fracture. Based on this, a pseudo-impact displacement of 1mm was used, with an example stack of MICs and delaminations introduced by the pseudo-impact shown in Fig. 5.

4.5 FEA models
Three models of impact damage were used in this study:

- Model-1: dent and delamination zones only, as per the analysis in Ref. (19)
- Model-2: dent, delamination and fibre fracture zones
- Model-3: dent, delamination, fibre fracture and pseudo-impact

5.0 Results
5.1 Experimental
Experimental results are presented for a specimen that best represents the average result from the repeat tests. An example of the XmCT scans is shown in Fig. 3, where an image was extracted of each ply as well as each interface between them. There was delamination found between each ply, and fibre fracture was found within the first six plies on the impacted side. Two specimens manufactured from the same larger panel underwent XmCT scans, as in order to achieve a high resolution the specimen was required
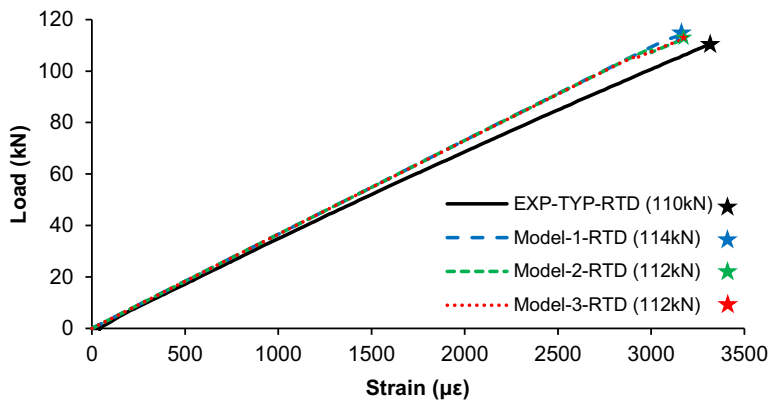
Figure 6. *Load-strain response from a typical experimental result (EXP-TYP) and FE models.*

to be cut to a smaller size: one was after the impact damage before any compressive loading (i.e. post-impact), and another specimen that was interrupted at approximately 95% of the expected failure load. The post-impact specimen had a total delamination area of 2,048mm^2 and the 95% loaded specimen had a total delamination area 2,420mm^2, representing an 18% growth in delamination.

5.2 Experimental vs numerical prediction

Figure 6 shows a comparison of the load-strain results of the three models and experimental results. Drops in the numerical results correspond to damage events The noticeable steps are the result of BSAM^{TM}'s method of damage initiation, where upon detection of damage initiation the displacement is paused and the damage is allowed to progress, resulting in an apparent drop in load at a specific displacement. For the experimental test, the residual strength was found to be 110kN, with coefficient of variation of 3.5% over nine specimens. Model-1 predicted a residual strength of 114kN, a 3.6% over-prediction; Model-2 predicted a residual strength of 112kN, a 1.8% over-prediction; and Model-3 predicted a residual strength of 112kN, a 1.8% over-prediction. The introduction of fibre fracture into the impact damage map led to reduction in predicted strength of 1.8% and the introduction of the pseudo-impact had no noticeable effect on the failure load of the predictions. However, all damage modes, (delamination, fibre fracture and matrix cracks) were seen to have initiated earlier in both models, particularly in the model with the pseudo-impact, as shown in the following sections.

6.0 Damage quantification

6.1 Delamination

The total delamination area of the models was calculated by using the sum of all cohesive interfaces that had failed at each step in the model and is shown in Fig. 7. One aspect of particular interest is that in Model-3 (which uses the pseudo-impact) the delamination area begins at approximately 2,200mm^2. This corresponds to the delamination area that is mapped into the model as weakened interfaces. The results are significant as they show that although each model has the same impact damage delamination map as weakened interfaces, there are large differences in when delamination initiates at these weakened interfaces and how delamination subsequently progresses. Model-1 (dent and delamination) only begins to initiate the mapped delamination at about 80% failure load, fully initiates at 95% and only progresses beyond the initial mapped area as the model reaches the failure load. Model-2 (which adds fibre fracture) begins delamination initiation at about 25% failure load, fully initiates at 85% load and then the delamination progresses further at 95% failure load. This shows that the addition of the fibre fracture
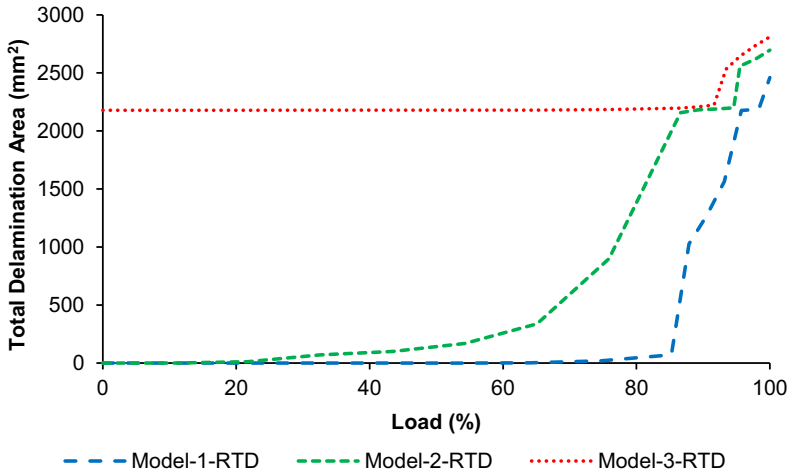
Figure 7. *Total delamination area vs load percentage of all three models.*
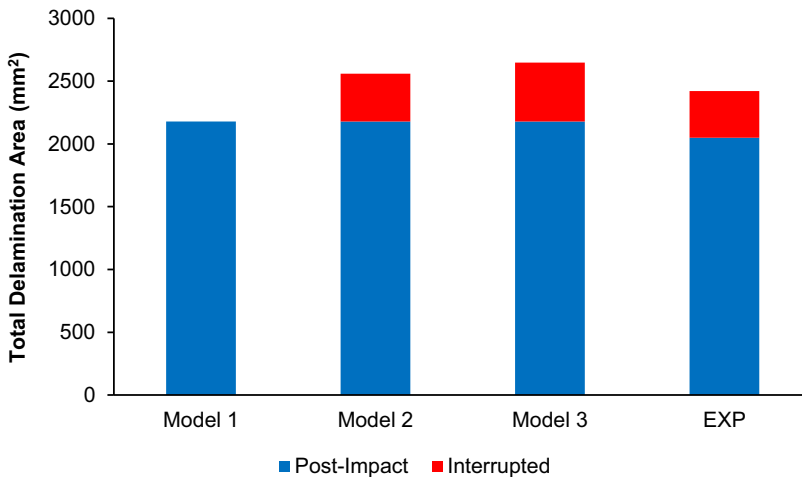

Figure 8. *Total delamination area of all three models and experiment (EXP).*

map has a large effect on the initiation and progression of the delamination, which is a critical damage mode interaction that demonstrates the necessity of incorporating fibre fracture into the impact damage map. The third model (which adds pseudo-impact) begins with the delamination map fully initiated and then shows delamination progression at 85% failure load. At the failure load the total amount of delamination area for models 1, 2 and 3, are 2,460, 2,696, and 2,811mm^2, respectively. The addition of the fibre fracture map led to a 10% increase in delamination area while the addition of the pseudo-impact stage led to a 14% increase in delamination area.

Figure 8 shows the total delamination area post-impact and at 95% failure load for experiment and all numerical models. Note that for the experimental results, the post-impact and 95% load results correspond to different specimens so are best interpreted as an estimate of growth, though delamination area across all specimens post-impact showed only small variation. It also can be seen that the experimental post-impact area differs from the model, this is because the map was taken from the scans of a different specimen. The model's map is translated to a mesh so there is change in area as the mesh does not align with the delamination shapes. Due to this discrepancy a different experimental specimen was chosen as
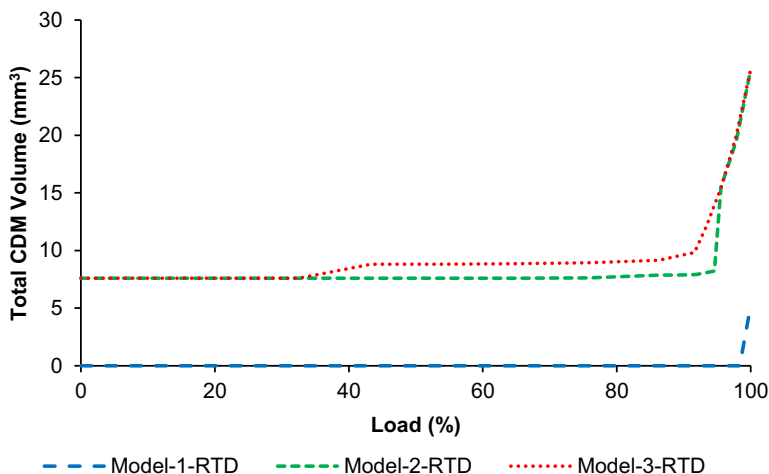
Figure 9. *Total fibre fracture CDM volume vs load percentage of all three models.*

it was manufactured from the same panel as the interrupted specimen, allowing for a closer comparison of experimental results. The experimental results show an estimated 18% increase in delamination area from post-impact to 95% load. In comparison, Model-1 (dent and delamination) showed no delamination growth at 95% load, Model-2 (fibre fracture added) showed a 17.5% growth while Model-3 (pseudo-impact added) showed a 21.5% growth. This shows that the numerical prediction accurately captures the delamination progression where fibre fracture was incorporated into the post-impact damage map, which reinforcing the critical linkage between fibre fracture and delamination.

6.2 Fibre fracture

Figure 9 shows the progression of fibre fracture damage, which was estimated using the total volume of all elements that had reached a CDM threshold of 0.25 (i.e. a degradation of material properties to 75% of original values). This threshold was determined from close inspection of the softening and subsequent progression of fibre fracture across elements. Model-1 (dent and delamination) showed fibre fracture only at final failure. Model-2 had the post-impact fibre fracture mapped and showed that fracture progressed slightly at 90% load with major growth seen at 95% load. Model-3 (pseudo-impact added) showed fibre fracture growing at 35% load and slightly further at 85% load with major fracture after 95% load. Although models 2 and 3 predicted around five times the fibre fracture volume, this only corresponded to a drop of around 2% in the failure load (as shown in Fig. 6).

6.3 Matrix cracking

The progression of the total length of all matrix cracks is shown in Fig. 10, which was calculated by finding the total area of MIC interfaces throughout the model and dividing by the ply thickness. The comparison of total matrix crack length between all three models shows the largest effect of introducing the pseudo-impact. Model-1 (dent and delamination) only initiates matrix cracking approaching the failure load of the prediction, while Model-2 (fibre fracture added) initiates matrix cracks at 95% load. Model-3 has matrix cracks introduced from the pseudo-impact, which then start to grow as early as 60% load and rapidly increase from 90% load. As the pseudo-impact model begins with initiation of matrix cracks, this allows the cracks to progress at a much earlier stage, which results in a much larger extent of cracking, and in turn provides more linkages to delamination damage initiation and growth.
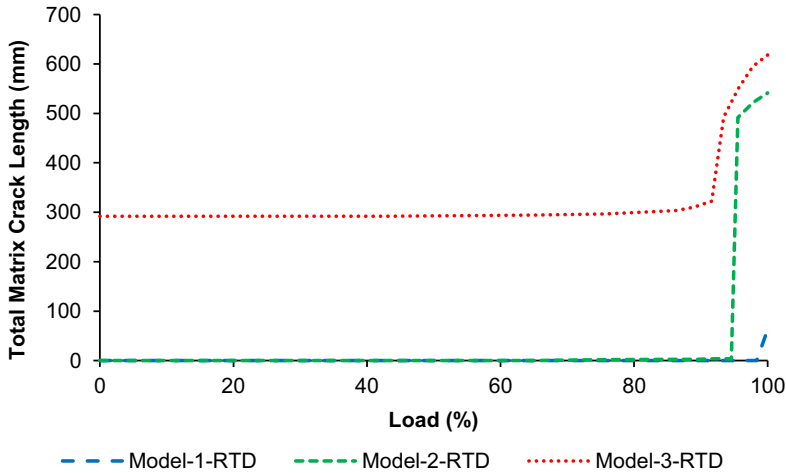
Figure 10. *Total matrix crack length vs load percentage of all three models.*
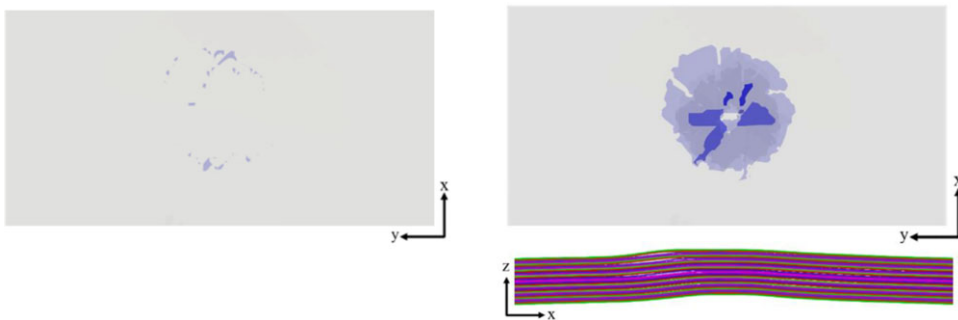

Figure 11. *Left: Delamination of Model-1 at 75% load. Right delamination (top) and 5× out-of-plane deformation cross-section (bottom) of Model-1 at 96% load.*

This shows that the pseudo-impact is vital in predicting all forms of damage progression and their interactions.

7.0 Damage progression breakdown

7.1 Model-1 – dent and delamination map only

Model-1 used a damage map in the form of a dent and the delamination zones as weakened interfaces. These weakened interfaces failed at 75% failure load, and at that stage no other damage had occurred. The delamination continued to progress and completely open by 96% failure load (Fig. 11). At this point no matrix cracks or fibre fracture had initiated, and the delaminations started to separate as the model deformed in the direction of the indentation.

At 100% load (Fig. 12) matrix cracks were introduced along the edges of delamination shapes, which allowed them to link across plies and form a cone of damage. The out-of-plane deformation continued to grow in the direction of the indentation. Minor fibre fracture softening occurred around the damage cone. Post-failure (Fig. 13) the matrix cracks continued to propagate and link with delaminations. The
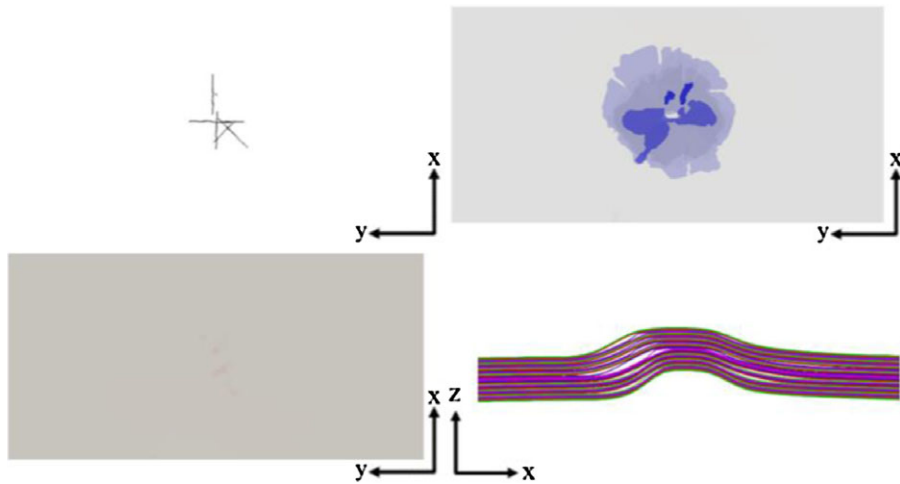
*Figure 12. Matrix cracks (top left), delamination (top right), fibre fracture (bottom left) and 5×
out-of-plane deformation cross-section (bottom right) of Model-1 at 100% load.*
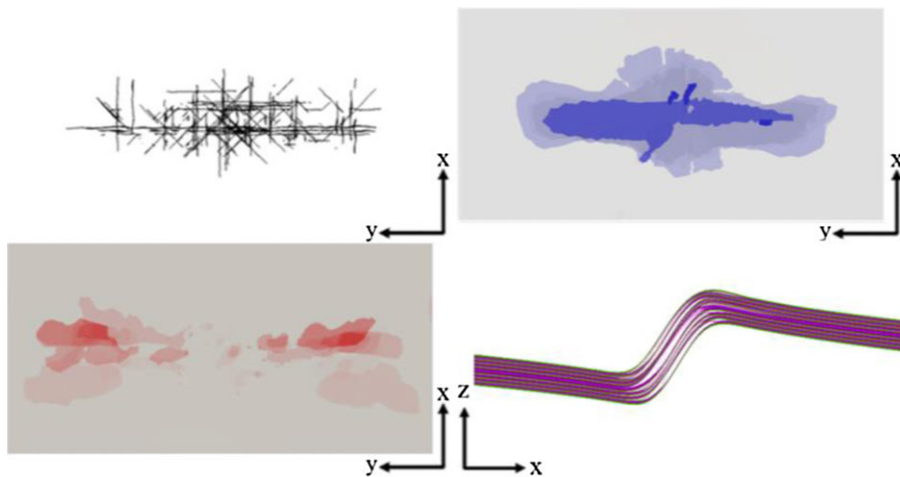

*Figure 13. Matrix cracks (top left), delamination (top right), fibre fracture (bottom left) and 5×
out-of-plane deformation cross-section (bottom right) of Model-1 post-failure.*

fibre fracture damage propagated from the centre out towards the edge. The panel stopped deforming
towards the indentation and buckled.

7.2 Model-2 – dent, delamination & fibre fracture map

Model-2 added the fibre fracture to the post-impact damage map. At 21% load (Fig. 14) the interfaces
closest to the impact face began to open, which was the only damage present.

By 87% load (Fig. 15) most of the mapped delaminations had initiated and a single matrix crack had
been introduced. Fibre fracture damage was beginning to propagate at the mapped crack tips and the
model slightly deformed in the direction of the indentation.

As the model progressed to 96% load (Fig. 16), several matrix cracks initiated and linked multiple
delaminations across plies as they propagated further. The fibre fracture continued to initiate around the
mapped fibre fractures and as the model deformed further the delaminations opened and began to spiral
through the thickness. This caused a sub-laminate buckle on the back face, which is shown in Fig. 17.
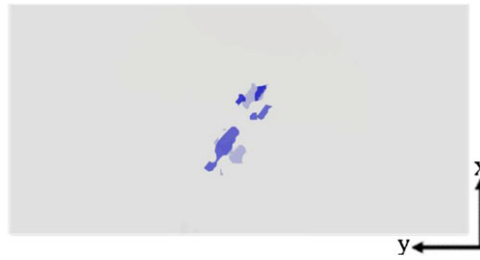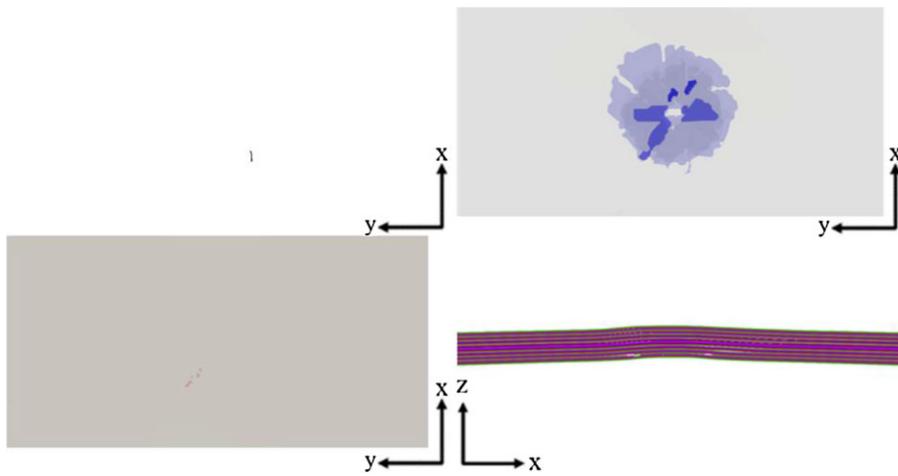
Figure 14. *Delamination of Model-2 at 21% load.*

Figure 15. *Matrix cracks (top left), delamination (top right), fibre fracture (bottom left) and 5× out-of-plane deformation cross-section (bottom right) of Model-2 at 87% load.*
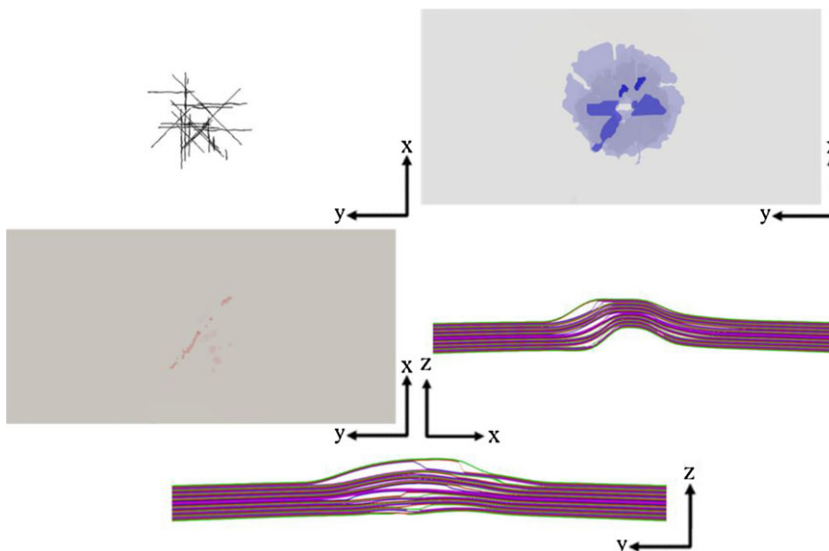

Figure 16. *Matrix cracks (top left), delamination (top right), fibre fracture (middle left), 5× out--of-plane deformation cross-section (middle right) and 5× out-of-plane deformation cross-section at sub-laminate buckle (bottom) of Model-2 at 96% load.*
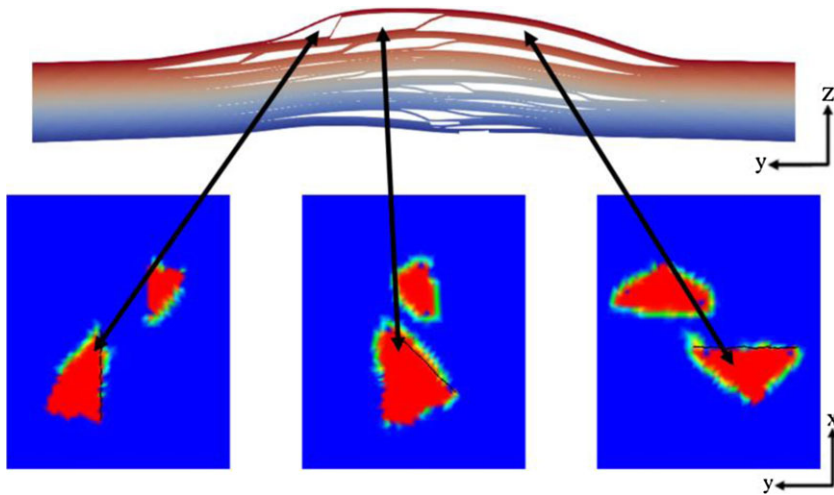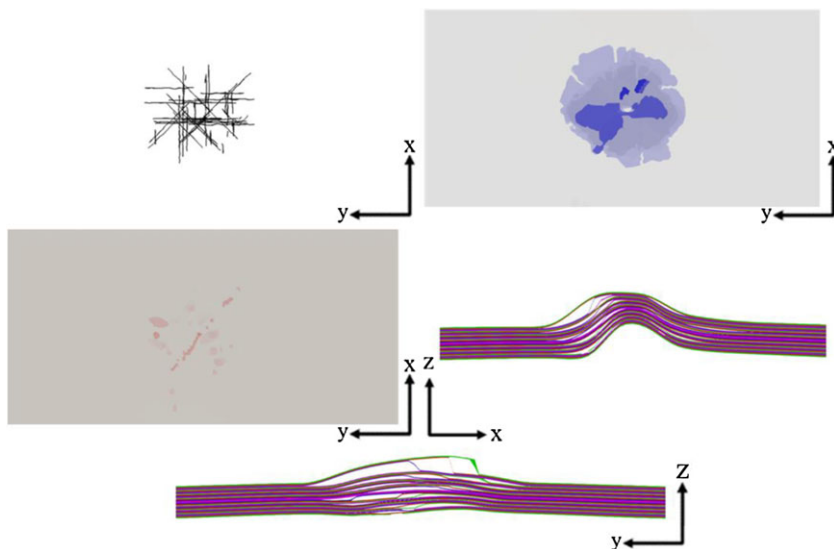
Figure 17. *ZY plane cross-section of the opening delaminations (5×) at 96% load with single interface delamination contours shown.*

Figure 18. *Matrix cracks (top left), delamination (top right), fibre fracture (middle left), 5× out-of-plane deformation cross-section (middle right) and 5× out-of-plane deformation cross-section at sub-lamina buckle (bottom) of Model-2 post-failure.*

As the model approached the maximum load the damage progressed, however, no new features were introduced. As the model continued past the max load (Fig. 18), the matrix cracking continued to grow with the delaminations towards the edges of the panel. The delaminations also continued to link and spiral through the thickness, causing to model to deform further towards the indentation. The fibre fracture damage propagated further and began to initiate at the edges of the deforming indentation.

7.3 Model-3 – pseudo-impact added

Model-3 added the pseudo-impact to all the previous damage maps. For this model by 33% load the sublaminate buckle described earlier began to appear (Fig. 19). This was due to the model starting with the delaminations already linked via matrix cracks, allowing them to deform much earlier than previously.

Figure 19. *5× out-of-plane deformation cross-section at sub-laminate buckle (bottom) of Model-3 at 33% load.*
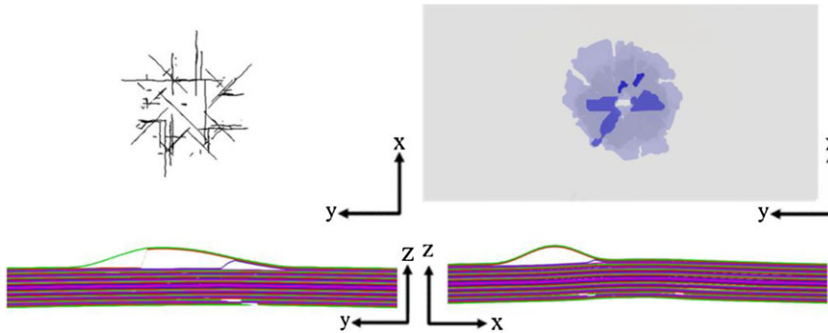

Figure 20. *Matrix cracks (top left), delamination (top right), 5× out-of-plane deformation cross-section at sub-lamina buckle (bottom left) and 5× out-of-plane deformation cross-section (bottom right) of Model-3 at 65% load.*
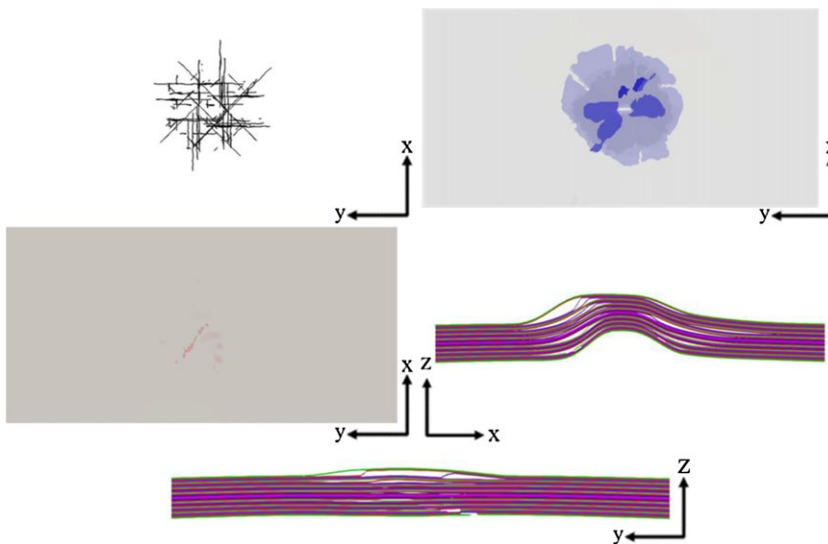

Figure 21. *Matrix cracks (top left), delamination (top right), fibre fracture (middle left), 5× out--of-plane deformation cross-section (middle right) and 5× out-of-plane deformation cross-section at sub-lamina buckle (bottom) of Model-3 at 96% load.*

By 65% this sub-laminate buckle had grown further and several delaminations were seen (Fig. 20) to spiral through the thickness of the model. This occurred before any delamination, fibre fracture or matrix cracks began to grow (Fig. 21).

As the model reached the max load (Fig. 22) the matrix cracking and delaminations began to grow towards the edges. The out-of-plane deformations rapidly grew in the direction of the indentations and
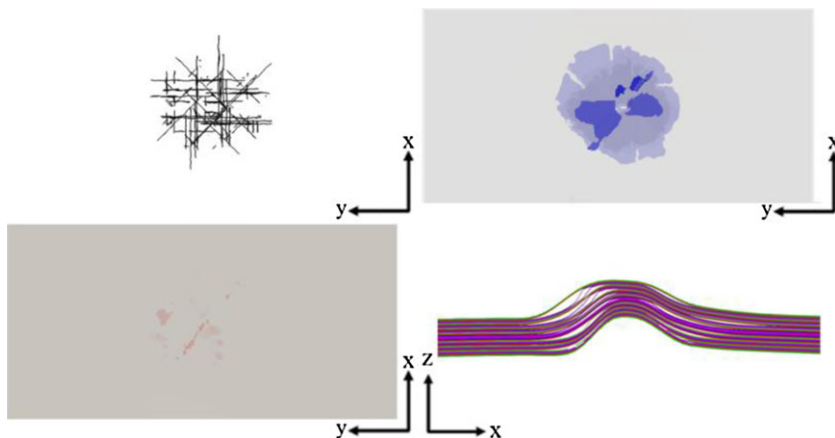
Figure 22. *Matrix cracks (top left), delamination (top right), fibre fracture (bottom left), and 5×
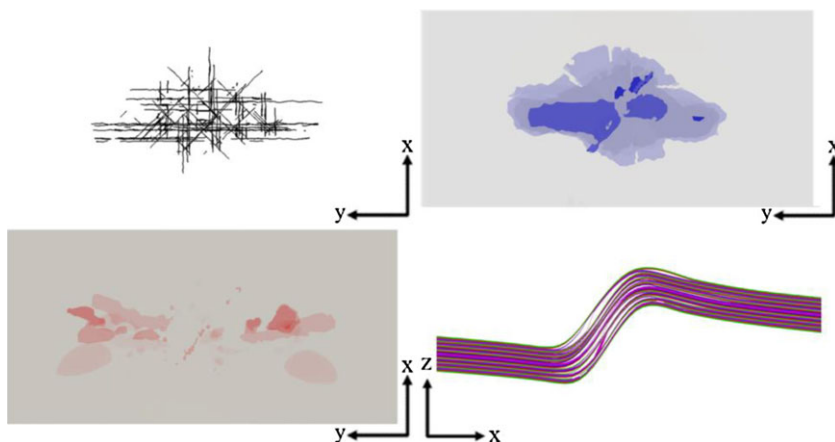out-of-plane deformation cross-section (bottom right) of Model-3 at max load.*

Figure 23. *Matrix cracks (top left), delamination (top right), fibre fracture (bottom left), and 5×
out-of-plane deformation cross-section (bottom right) of Model-3 post-failure.*

fibre fracture damage was introduced at the edges of the deformation and continued to progress around
the mapped fractures.

Post-failure (Fig. 23), the matrix cracks and delaminations progressed outwards until the panel buck-
led. The fibre fracture that initiated around the deformation rapidly progressed outwards, with the critical
fibre fracture damage occurring on the 0 degrees plies. The panel then buckled and completely failed.

7.4 Experimental vs numerical prediction

Figures 24 and 25 show a comparison of experimental and numerical delamination between each ply as
the initial damage, post-impact prior to compressive loading, and final damage, interrupted at 95% load.
As previously mentioned, the experimental results are of two different specimens (labelled "21-14" and
"21-15"), as in order to achieve a high-quality scan the specimen needed to be cut down, rendering it
unable to undergo any further testing.

Due to this there is an apparent decrease in delamination in several plies, however, this typically
occurred next to a larger than average increase in delamination, indicating the apparent decrease is
due to potential delamination progression propagating across plies via matrix cracking. The numerical
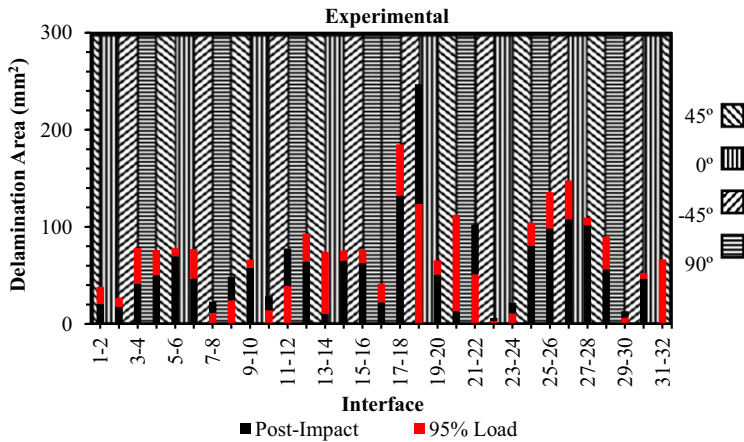
Figure 24. *Experimental delamination area post-impact at each ply interface, specimen 21-14 (initial damage) and at 95% load, specimen 21-15 (final damage).*
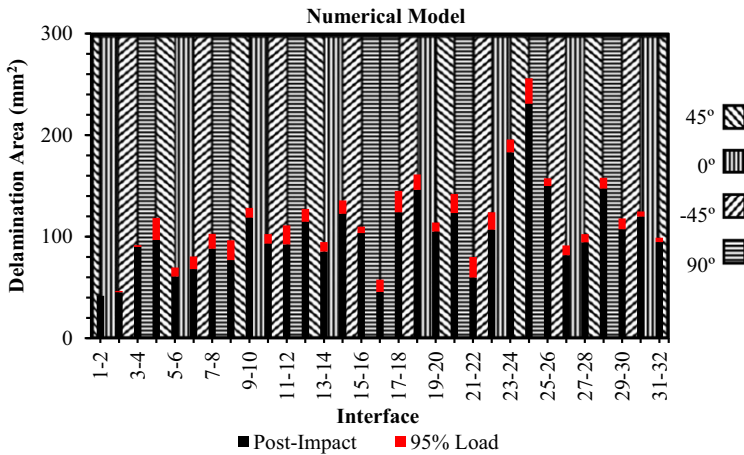

Figure 25. *Numerically predicted delamination area post-impact (initial damage) and at 95% load (final damage) in Model-3.*

results are from Model-3, as it this was considered the most suitable modelling strategy according to the previous comparisons. The experimental results show that the delamination tended to propagate across the entire specimen at a relatively similar rate, this is also seen in the numerical prediction, however, with a slight inclination towards the centre of the specimen.

8.0 Conclusion

An investigation into the residual strength and damage progression of a compression after impact specimen was conducted using the high-fidelity finite element tool BSAM™. The analysis incorporated an impact damage map, which characterised the indentation, delamination and fibre fracture, as well as an initial pre-load used to initiate delamination and matrix cracking. The inclusion of initial fibre fracture into the impact damage map was found to have a small decrease in residual strength, however, there was a noticeable change in damage progression at low loads. The addition of a pseudo-impact pre-load was found to have little effect on the failure load, however, the damage progression of the prediction was found to have a much larger amount of both delamination and matrix cracking, especially at low to

moderate loads. Importantly, there was shown to be strong interaction between all damage modes, and all were needed to be included in the numerical model as part of the post-impact damage map. Scans of a specimen post-impact and pre-failure (∼95% failure load) were compared to investigate the extent of delamination progression and it was found that the numerical model predicted a similar amount of propagation prior to failure. These results imply that, given a critical damage pattern, these methods could be vital in predicting the damage progression of composite materials.

References

[1] Soutis, C. and Curtis, P.T. Prediction of the post-impact compressive strength of CFRP laminated composites, *Compos. Sci. Technol.*, 1996, **56**, (6), pp 677–684, doi: 10.1016/0266-3538(96)00050-4

[2] Turon, A., Dávila, C.G., Camanho, P.P. and Costa, J. An engineering solution for mesh size effects in the simulation of delamination using cohesive zone models, *Eng. Fract. Mech.*, 2007, **74**, (10), pp 1665–1682, doi: 10.1016/j.engfracmech.2006.08.025

[3] Maimí, P., Camanho, P.P., Mayugo, J.A. and Dávila, C.G. A continuum damage model for composite laminates: Part I - Constitutive model, *Mech. Mater.*, 2007, **39**, (10), pp 897–908, doi: 10.1016/j.mechmat.2007.03.005

[4] Swindeman, M.J., Iarve, E.V., Brockman, R.A., Mollenhauer, D.H. and Hallett, S.R. Strength prediction in open hole composite laminates by using discrete damage modeling, *AIAA J.*, 2013, **51**, (4), pp 936–945, doi: 10.2514/1.J051773

[5] Mendes, P.A.A.E. and Donadon, M.V. Numerical prediction of compression after impact behavior of woven composite laminates, *Compos. Struct.*, 2014, **113**, (1), pp 476–491, doi: 10.1016/j.compstruct.2014.03.051

[6] Dubary, N., Bouvet, C., Rivallant, S. and Ratsifandrihana, L. Damage tolerance of an impacted composite laminate, *Compos. Struct.*, 2018, **206**, pp 261–271, doi: 10.1016/j.compstruct.2018.08.045

[7] Sun, X.C. and Hallett, S.R. Failure mechanisms and damage evolution of laminated composites under compression after impact (CAI): Experimental and numerical study, *Compos. Part A Appl. Sci. Manuf.*, 2018, **104**, pp 41–59, doi: 10.1016/j.compositesa.2017.10.026

[8] Liu, H., Falzon, B.G. and Tan, W. Predicting the Compression-After-Impact (CAI) strength of damage-tolerant hybrid uni-directional/woven carbon-fibre reinforced composite laminates, *Compos. Part A Appl. Sci. Manuf.*, 2018, **105**, pp 189–202, doi: 10.1016/j.compositesa.2017.11.021

[9] Tuo, H., Lu, Z., Ma, X., Zhang, C. and Chen, S. An experimental and numerical investigation on low-velocity impact damage and compression-after-impact behavior of composite laminates, *Compos. Part B Eng.*, 2019, **167**, pp 329–341, doi: 10.1016/j.compositesb.2018.12.043

[10] Lin, S. and Waas, A.M. Accelerating computational analyses of low velocity impact and compression after impact of laminated composite materials, *Compos. Struct.*, 2021, **260**, Art no. 113456, doi: 10.1016/j.compstruct.2020.113456

[11] Suemasu, H. and Kumagai, T. Compressive behavior of multiply delaminated composite laminates part 2: Finite element analysis, *AIAA J.*, 1998, **36**, (7), pp 1286–1290, doi: 10.2514/2.512

[12] Moura, M.F.S.F., Gonçalves, J.P.M., Marques, A.T. and Castro, P.M.S.T. Prediction of compressive strength of carbon-epoxy laminates containing delamination by using a mixed-mode damage model, *Compos. Struct.*, 2000, **50**, (2), pp 151–157, doi: 10.1016/S0263-8223(00)00091-X

[13] Craven, R., Iannucci, L. and Olsson, R. Delamination buckling: A finite element study with realistic delamination shapes, multiple delaminations and fibre fracture cracks, *Compos. Part A Appl. Sci. Manuf.*, 2010, **41**, (5), pp 684–692, doi: 10.1016/j.compositesa.2010.01.019

[14] Bull, D.J., Spearing, S.M. and Sinclair, I. Image-enhanced modelling of residual compressive after impact strength in laminated composites, *Compos. Struct.*, 2018, **192**, pp 20–27, doi: 10.1016/j.compstruct.2018.02.047

[15] McQuien, J.S., Hoos, K.H., Ferguson, L.A., Iarve, E.V. and Mollenhauer, D.H. Geometrically nonlinear regularized extended finite element analysis of compression after impact in composite laminates, *Compos. Part A Appl. Sci. Manuf.*, 2020, **134**, Art no. 105907, doi: 10.1016/j.compositesa.2020.105907

[16] Iarve, E.V. Mesh independent modelling of cracks by using higher order shape functions, Int. J. Numer. Methods Eng., 2003, 56, (6), pp 869–882, doi: 10.1002/nme.596

[17] Iarve, E.V., Gurvich, M.R., Mollenhauer, D.H., Rose, C.A. and Dávila, C.G. Mesh-independent matrix cracking and delamination modeling in laminated composites, *Int. J. Numer. Methods Eng.*, 2011, **88**, (8), pp 749–773, doi: 10.1002/nme.3195

[18] Pinho, S.T.D., Davila, C.G., Camanho, P.P., Iannucci, L. and Robinson, P. *Failure Models and Criteria for FRP Under In-Plane or Three-Dimensional Stress States Including Shear Non-Linearity,* National Aeronautics and Space Administration, NASA Langley Research Center, 2005, Hampton, VA, 23681-2199, L-19089, 01/02/2005.

[19] Harman, A.B., et al. Numerical assessment of compression strength after impact for impact for enhanced aircraft sustainment, *Proceedings of the American Society for Composites - 34th Technical Conference, ASC 2019*, 2019.

[20] ASTM, D7137/D7137M - 17 Standard Test Method for Compressive Residual Strength Properties of Damaged Polymer Matrix Composite Plates.